Understanding seismic waves generated by train traffic via modelling: implications for seismic imaging and monitoring

Supplemental Material

François Lavoué, Olivier Coutant, Pierre Boué,
Laura Pinzon-Rincon, Florent Brenguier, Romain Brossier,
Philippe Dales, Meysam Rezaeifar, and Christopher J. Bean

Contents

Description of the Supplemental Material

This Supplemental Material gives more insights into some aspects of the study that could not be fully developed in the paper:

1. *Effect of ground stiffness on the amplitude of the loading force:* for the sake of completeness, we give the expressions of track deflection and (again) of the reaction force exerted on a deflected track, as given by the Euler-Bernoulli elastic beam (E-BEB) model. While Fig. 3 in the main text depicted the reaction forces with normalised amplitudes, in order to discuss the effect of ground stiffness on the width of the function and on the high-frequency content of the resulting spectra, Fig. S1 presents non-normalised displacements and forces to illustrate the non-linear effect of ground stiffness on the magnitude of the applied force, and therefore on the amplitude of the recorded ground velocities.

2. *Signal amplitudes vs. train length and train speed:* Figures S2 and S3 come in support of the discussion about the general behaviour of amplitudes with respect to the number of wheel loads and train speed.

3. *More examples of signals dominated by the signature of moving loads:* our choice of train parameters in the experiments shown in Fig. 4 aims at presenting the examples that best illustrate the underlying mechanisms (single stationary source vs. single moving load) and best explain the observations (Figs 4b,e), but it makes the comparison between Figs 4(a,c) and Figs 4(d,f) not straightforward. For the sake of completeness, we present more results in Fig. S4 for one-to-one comparison.

4. *Effect of seismic properties, distance from railway, and wave types:* Figures S5 and S6 show the effect of seismic velocities and attenuation, of the distance between the sensor and the railway, and of the considered wave types (depending on whether the convolutions with the source time functions are applied to all arrivals, including surface waves, or to first arrivals only, i.e. to refracted body waves).

For the sake of reproducibility, the Python notebooks used to perform the convolutions of the Green functions with the source time functions representing the train passages can be found here: `https://gricad-gitlab.univ-grenoble-alpes.fr/pacific/publications/2020_Lavoue-et-al_SRL_supplemental-material`. Unlike the paper and this PDF, these codes are susceptible to evolve based on future developments and user feedback (please feel free to provide feedback!).

List of Figures

Supplemental Text

Effect of ground stiffness on the amplitude of the loading force

Figure S1 shows the displacement and reaction force of a deflected track according to the Euler-Bernoulli elastic beam (E-BEB) model for several values of ground stiffness. Note that, since we consider a weight $F_i = 100$ kN here, the reaction force values (in kN, in red) are also representative of the percentage (in %) of the load transferred to the ground.

The stiffer the ground beneath the rail is, the narrower the spatial loading function, thus the more high-frequency in the resulting signals, the smaller the deflection (in blue), and the larger the vertical force exerted by the track on the ground (in red). The magnitude of the vertical force P_j acting on the sleepers therefore increases linearly with axle load F_i (see eq. S2 below) and non-linearly with ground stiffness α (except for the quasi-static component which depends only on axle load).

As a reminder, the expressions of the deflection and reaction force of a track described by the E-BEB model are (Krylov and Ferguson, 1994, eqs 2 and 7; Li et al., 2018, eqs 2-3):

$$w_j(x_i) = \frac{F_i\beta}{2\alpha}\, e^{-\beta|x_i - x_j|}\big[\cos\big(\beta|x_i - x_j|\big) + \sin(\beta|x_i - x_j|)\big], \tag{S1}$$

$$P_j(x_i) = 2F_i\, e^{-\beta|x_i - x_j|}\,\Big[\cos\big(\beta|x_i - x_j|\big) + \sin(\beta|x_i - x_j|)\Big]\;\frac{\Delta_{sleeper}}{x_0}, \tag{S2}$$

with

- $w_j(x_i)$ the deflection of sleeper j due to wheel i (in m),
- $P_j(x_i)$ the reaction force of sleeper j due to wheel i (in N),
- x_i and x_j the positions (in m) of wheel i and sleeper j along the rail, respectively,
- $F_i = m_i\, g$ the load of wheel axle i (in N), derived from the *load* (i.e. mass m_i, in kg) reported by Fuchs et al. (2018) and in train specifications [typically of the order of 150 kN / 15 tons],
- $\Delta_{sleeper}$ the sleeper spacing (in m) [$\Delta_{sleeper} = 24" = 0.6096$ m in our experiments],
- $x_0 = \pi/\beta$ the total deflection distance (in m, Krylov and Ferguson, 1994),
- $\beta = (\alpha/4EI)^{0.25}$ (in m^{-1}), with
  - E the elastic modulus (in N/m^2) and I the cross-sectional momentum (in m^4) of the rail,
  - α the ground stiffness (in N/m^2).

Typical values for the latter quantities are $E \simeq 2.10^{11}$ N/m^2, $EI = 58.5$ MN.m^2, and $\alpha = 10$ MN/m^2 (Li et al., 2018), or $\alpha = 61.8$ MN/m^2 (Krylov and Ferguson, 1994). In our experiments, we consider $\alpha = 800$ MN/m^2, which corresponds to a rather stiff soil but matches the width of the triangular spatial window given by Paderno (2009) and —more importantly— the seismic observations of Fuchs et al. (2018) (see Figs 4b,c in the main text).

Signal amplitudes vs. train length

Figure S2 shows seismograms and spectra resulting from trains with an increasing number of axle loads (following the geometry of Fig. 1a and the values of Table 1), travelling at 120 km/h over slightly irregular sleepers ($\Delta_{sleeper} = 0.6096 \pm 0.05$ m). This provides an alternative to Fig. 2 in illustrating the progressive build-up of a train and the distinct roles of its different characteristic lengths (Fig. 1a) in the resulting spectra.

- Fig. S2(c): With 1 wheel axle (single moving load), the spectrum is dominated by (i) the spectrum of the Green function G_{zz} convolved by the loading function (Fig. 3), and (ii) by the sleeper passage frequency $f_2 = V_{train}/\Delta_{sleeper}$ controlled by train speed and sleeper spacing, typical of a moving load.
- Fig. S2(e): With 2 wheel axles, the spectrum is modulated by the frequency $f_a = V_{train}/\Delta_a$ controlled by the train speed and the distance Δ_a between axles within one bogie (pink dotted lines in Fig. S2, see also the black dotted lines in Fig. 2).
- Fig. S2(g): With 4 wheel axles, the spectrum is further modulated by the frequency $f_{b_1} = V_{train}/\Delta_{b_1}$ controlled by the train speed and the distance Δ_{b_1} between two bogies within one wagon (purple dashed lines in Fig. S2, see also the black dashed lines in Fig. 2).
- Fig. S2(i): With 8 wheel axles (2 wagons), peaks appear at frequency $f_1 = V_{train}/L_w$ related to train speed and wagon length L_w. Note that, while these peaks are modulated by the previous frequencies f_a and f_{b_1}, they well correspond to frequency f_1, i.e. they are different from the previous f_{b_1}-peaks, which are less peaks than sharp modulations.
- Figs S2(k,m): When adding more wheel axles (4, 8, 32 wagons), the periodicity due to wagon length is enhanced (less frequency leakage), so peaks at frequency f_1 become sharper and sharper, but they remain modulated by frequencies f_a and f_{b_1}, as expected from Fig. 2. Also note how the asymmetry of the signal envelope increases with the number of wheel axles (Fig. S2a,b,d,f,h,j,l), which is an effect of the length of the train on the total duration of the signal and on the interferences that are generated.

Figures S2(n,o) show the evolution of the maximum amplitude of the time-domain signals (n) and of the spectral energy in given frequency bandwidths (o) as a function of the number of wheel loads. Time-domain amplitudes increase approximately as $\sqrt{N}$ with the number of wheel loads N. We understand this trend as partly due to the time derivative relating displacements to ground velocities (maximum displacement amplitudes are approximately proportional to the number of wheel loads, as expected from eq. S1 and from the linearity of the wave equation with respect to the source term), while we interpret the deviations to the trend as being due to the interferences between the waves generated by the different wheels and sleepers, which introduce some non-linearity. Similarly, the spectral energy computed either in the full ([0 - 100] Hz) or in a restricted ([1 - 20] Hz) frequency bandwidth increases (almost exactly) linearly with the number of wheel loads, which again is expected from the source time functions that represent the energy that we inject in the system.

Signal amplitudes vs. train speed

Figure S3 shows seismograms and spectra resulting from trains travelling at increasing speeds over slightly irregular sleepers ($\Delta_{sleeper} = 0.6096 \pm 0.05$ m). This illustrates the effect of train speed on the fundamental frequencies which are shifted towards higher values for increasing speeds. Note however that the spectra are not only stretched towards higher frequencies but that their shapes also change with train speed, which we interpret as the effect of the non-stationary interferences between the waves generated by the different wheels and sleepers.

Signal amplitude and energy increase with train speed: faster trains make more noise. Note however that this is true for ground velocities (shown here) but not for displacements (not shown), which are dominated by the static effect of the weight of the train: according to our mechanism of quasi-static axle load, the maximum displacement is therefore constant with respect to train speed.

Contrary to the effect of the number of wheel loads (Fig. S2), the evolution of amplitudes and energy is not fully understood. We can nevertheless observe that the maximum time-domain amplitude and the total signal energy seem to lie in between a linear and a quadratic trend with respect to train speed (Fig. S3l,m).

Before computing energies in finite frequency bands, it should be noted that a given frequency band does not encompass the same proportion of the spectrum for different train speeds. Due to the *stretching* effect of increasing train speeds, energy tends to leak out of fixed frequency bands (e.g. [1 - 20] Hz) as train speed increases. On the other hand, frequency bands of the form $[\ k - 0.5\ ,\ k + 0.5\ ]\ f_a$, that evolve proportionally with train speeds since $f_a = V_{train}/\Delta_a$, always contain approximately the same proportion of the spectrum, which brings us back to our *rule of thumb* stating that most of the energy of train-generated signals is expected to be in the [0.5 - 1.5] f_a frequency band controlled by train speed and axle distance Δ_a within each bogie. A direct implication of this for detecting train-generated signals in seismic records is that the considered frequency band should be adapted to the estimated speed of the trains generating these signals.

Again, we remind that our modelling does not account for dynamic excitation effects which, in reality, also contribute to the fact that faster trains make more noise. Also, our trains are quite slow ($V_{train} \leq 35$ m/s) compared to the seismic velocities of the medium ($v_{Rayleigh} \simeq 2700$ m/s). High-speed trains ($V_{train} \simeq 100$ m/s) travelling at near-critical speeds over low-velocity media ($v_{Rayleigh} \simeq 200$ m/s) also generate higher-amplitude vibrations (e.g. Lombaert and Degrande, 2009; Alves Costa et al., 2010; Galvín et al., 2010).

More examples of signals dominated by the signature of moving loads

Figure S4 presents synthetic signals resulting from train passages over exactly regular sleepers, and therefore dominated by the signature of a single moving load and by frequency $f_2 = V_{train}/\Delta_{sleeper}$. Here we assume a train length $L_w = 26.5$ m and a train speed $V_{train} = 33.125$ m/s $= 119.25$ km/h, such that $f_1 = 1.25$ Hz, as observed by Fuchs et al. (2018) at AlpArray station A002A (see Fig. 4b in the main text).

Figure S4(a) is very similar to Fig. 4(a) in the main text, the only difference being a higher train speed that reduces the duration of the signal and increases the frequency f_2 and the Doppler frequency shift.

Figure S4(b) can be compared to Fig. 4(c) in the main text. The only difference is that Fig. S4(b) results from perfectly regular sleepers while Fig. 4(c) considered slightly irregular sleepers. Fig. S4(b) demonstrates that perfectly regular sleepers generate a signal that is clearly dominated by the signature of a single moving load. The frequency peaks expected at multiples of the frequency f_1 related to wagon periodicity are not visible at all in the spectrum.

Finally, Figs S4(c) and (d) present signals generated by a single wheel axle (Figs S4c) and a full 8-wagon train (Figs S4d) travelling over sleepers with a larger spacing, retaining every 19 sleeper. Figure S4(d) therefore differs from Fig. 4(f) only by the considered train speed, and also displays a signal that is dominated by the signature of a single moving load (Figs S4c), with a frequency line spacing $f_2/19$.

Effect of seismic properties, distance from railway, and wave types

Figure S5 presents results obtained in different configurations. Figure S5(a) is our reference case, using the settings described in Table 1 (same as Fig. 4c in the main text). Figure S5(b) presents the signal obtained by assuming a sensor located further away from the railway (d_{min} = 1200 m instead of 300 m). As expected, wave propagation over a longer distance results (i) in a relative decay of high frequencies in the spectrum, and (ii) in a longer apparent duration of the signal: because of the relative decay of amplitudes due to attenuation and geometrical spreading, a sensor located further away from the railway *sees* a larger number of sources contributing with an equivalent importance. Note also the slightly smaller Doppler frequency shift affecting the spectral line associated to frequency f_2, due to the larger angle between the sensor and the train trajectory, resulting in a slower apparent train speed.

Figure S5(c) illustrates the effect of seismic velocities: assuming higher velocities (V_P = 5000 m/s instead of 3400 m/s and V_S = 3000 m/s instead of 2000 m/s) also results in a longer apparent duration of the signal, which can also be explained in terms of relative decay of amplitudes due to geometrical spreading over a smaller number of longer wavelengths. Note also the lower amplitudes in Fig. S5(c) compared to Fig. S5(a), due to the fact that the amplitude of surface waves is enhanced in soft, low-velocity media (which is probably one of the reasons why the amplitudes of observed train-generated signals are larger than our synthetic amplitudes, obtained for seismic velocities that have been chosen artificially high to mitigate computation costs). Finally, the Doppler frequency shift affecting the spectral line associated to frequency f_2 is also decreased compared to Fig. S5(a), due to the larger discrepancy between the seismic (Rayleigh) velocity and the (apparent) train speed.

Finally, Figure S5(d) illustrates the effect of seismic attenuation on the signals: as expected, assuming larger quality factors (Q_P = 500 instead of 100 and Q_S = 200 instead of 50) results in slightly higher amplitudes, especially at early and late times corresponding to the furthest source locations, resulting in a longer apparent duration of the signal (but, surprisingly, does not change much the maximum amplitude recorded when the train is closest to the sensor). Higher quality factors also better preserve the high-frequency content in the spectra.

Figure S6 shows the results obtained in a medium where seismic velocities increase with depth, giving rise to refracted body waves, and compares (a) the signal resulting from the convolution of all arrivals (dominated by surface waves) with the train source time functions and (b) the signal resulting from the convolution of the refracted P waves (first arrivals) only. The latter aims at mimicking long-distance wave propagation in heterogeneous media where high-frequency surface waves would vanish due to strong scattering in the shallow subsurface, which is difficult to reproduce in our synthetic simulations.

Of course, convolving small-amplitude body waves (Fig. S6b) results in smaller amplitudes than considering high-amplitude surface waves (Fig. S6a), but both results present very similar spectral characteristics. Apart from a very low-frequency (quasi-static) component that is present in (b) and not in (a) [which is not very well understood and might be due to our preprocessing], the two spectrograms are nearly identical, suggesting that the conclusions of our study, although mostly based on short-distance signals dominated by surface waves, remain valid for long-distance body waves.

It is also worth noticing that Fig. S6(a) is very similar to Fig. S5(d), obtained in the same configuration but in a homogeneous medium, suggesting that medium structure plays little role in the pattern of the resulting signal, which complexity mostly comes from the source, i.e. from the source time functions and from the interferences between waves generated by the many sources involved.

Supplemental Figures

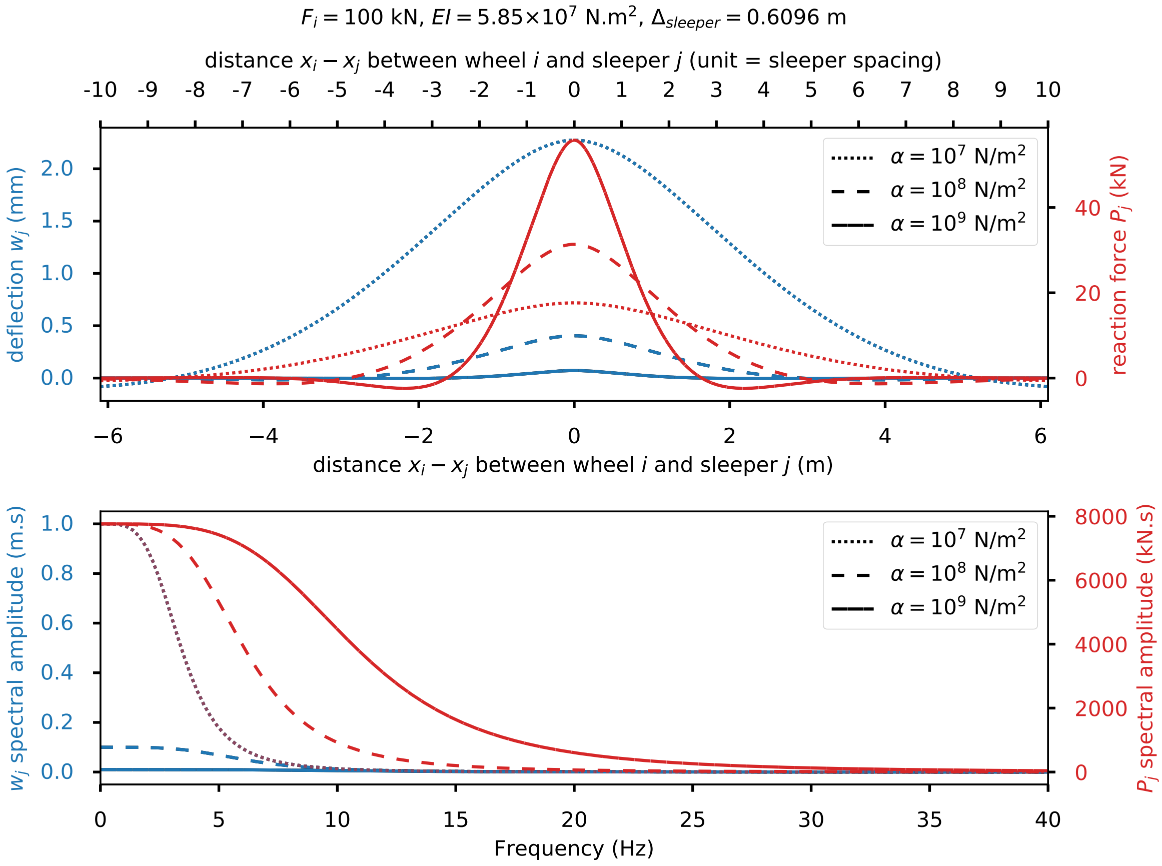

Figure S1: Top: Displacement (in blue) and reaction force (in red) of a deflected track according to the Euler-Bernoulli elastic beam model (E-BEB, eqs S1, S2) for several values of ground stiffness α (solid, dashed and dotted lines). Note that, since we consider a weight $F_i = 100$ kN here, the reaction force values (in kN, in red) are also representative of the percentage (in %) of the load transferred to the ground. Bottom: Related spectra, assuming a train speed of 120 km/h for space-to-time conversion.

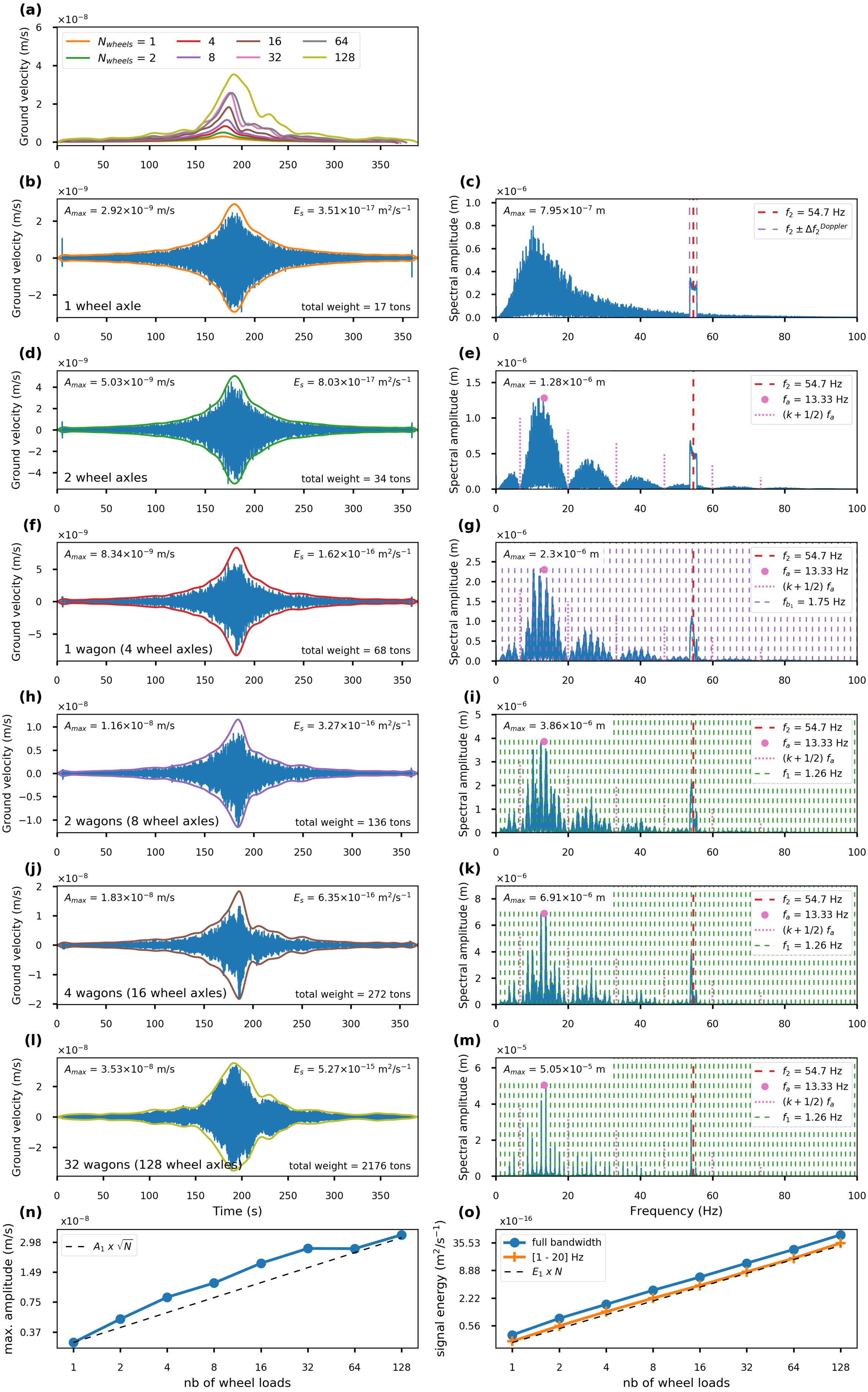

Figure S2: Seismograms (left) and spectra (right) resulting from trains with increasing number of axle loads, travelling at 120 km/h over slightly irregular sleepers (b-m). The top figure (a) compares the envelopes of the signals. Bottom panels show the evolution of the maximum amplitude of the time-domain signals (n) and of their spectral energy (o) as a function of the number of wheel loads (note the $\log_2$ axes).

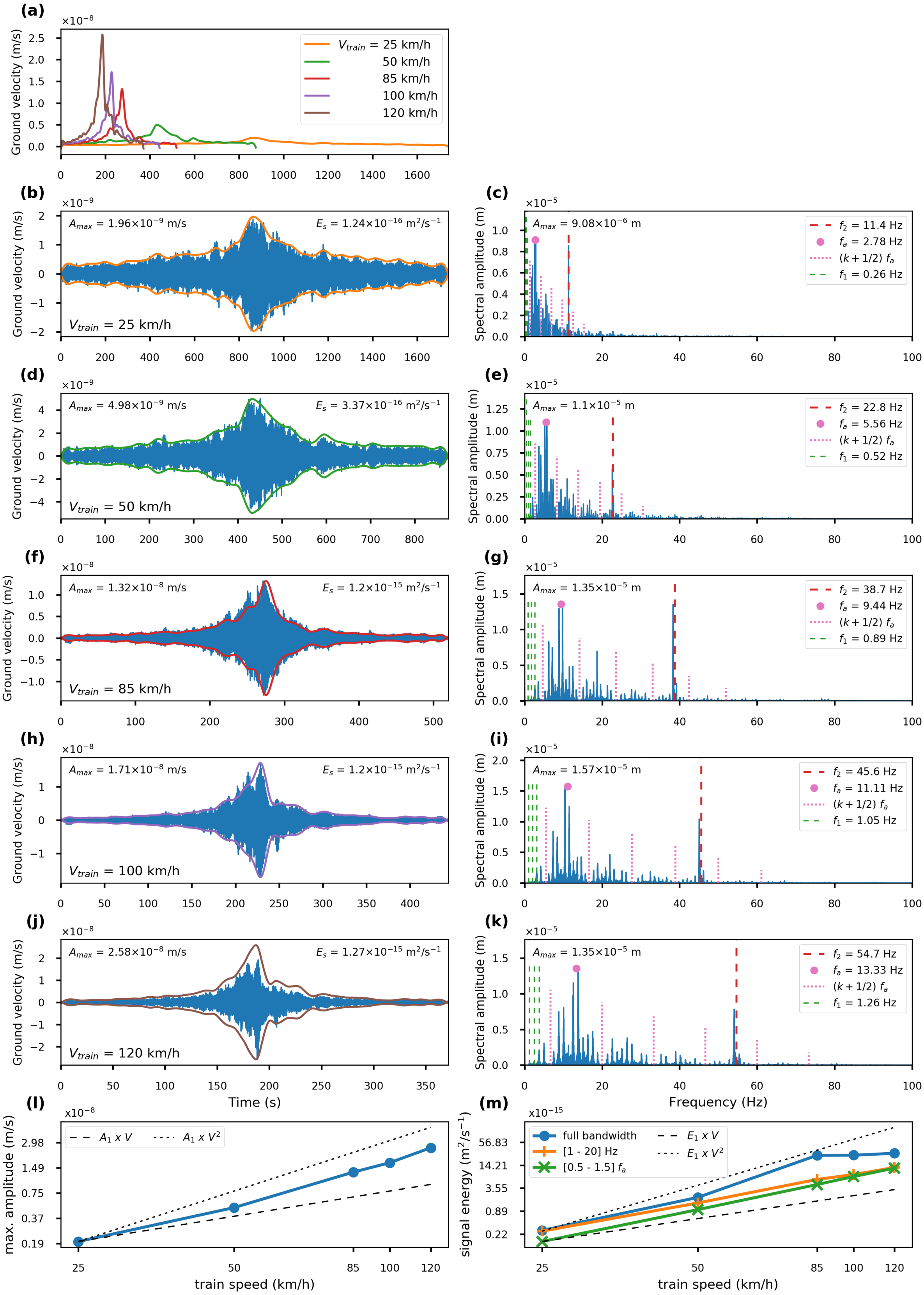

Figure S3: Seismograms (left) and spectra (right) resulting from trains travelling at increasing speeds over slightly irregular sleepers (b-k). The top figure (a) compares the envelopes of the signals on a common time axis. The bottom figures show the evolution of the maximum amplitude of the time-domain signals (l) and of their spectral energy (m) as a function of train speed (note the $\log_2$ axes).

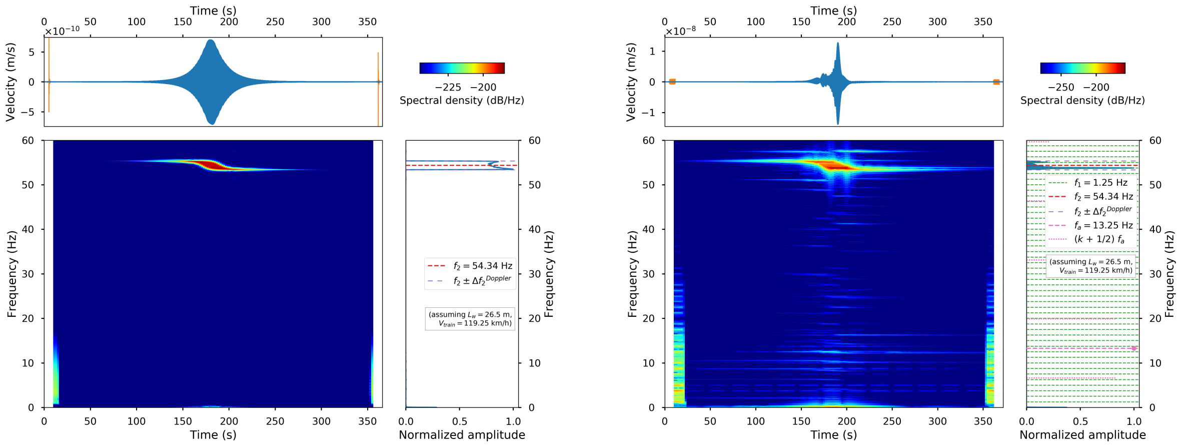

(a) Single moving load on perfectly regular sleepers.

(b) All wheels, all sleepers, perfectly regular sleepers.

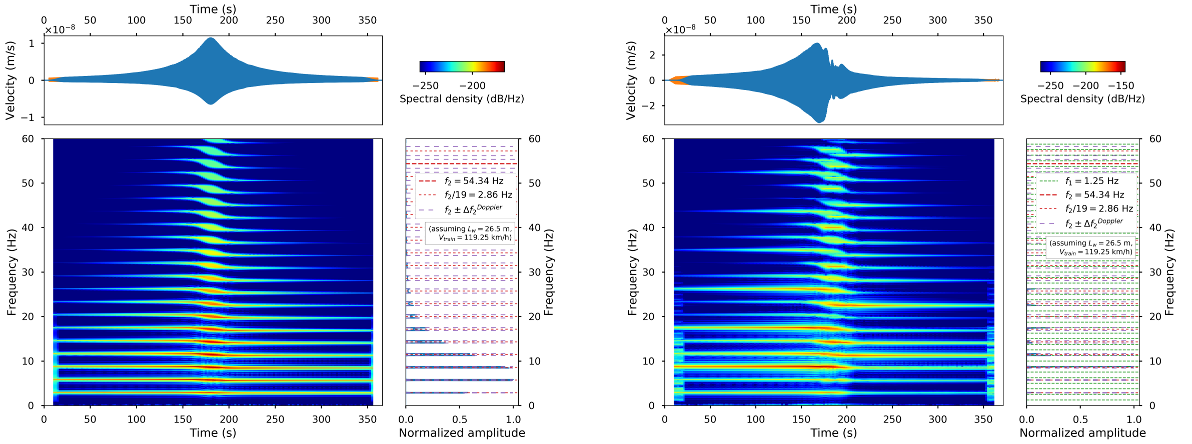

(c) Single moving load on perfectly regular sleepers (every 19 sleeper).

(d) All wheels, every 19 sleeper, perfectly regular sleepers.

Figure S4: Seismograms (top of each panel), spectrograms (bottom of each panel) and spectra (right of each panel) resulting from train passages over exactly regular sleepers, and therefore dominated by the signature of a single moving load. The first row (panels a, b) considers all sleepers spaced every $\Delta_{sleeper} = 0.6096$ m, resulting in a passage frequency $f_2 = V_{train}/\Delta_{sleeper}$, while the second row considers only every 19 sleeper, resulting in a passage frequency $f_2' = f_2/19$. All figures assume a train speed $V_{train} = 33.125$ m/s $= 119.25$ km/h. Panels (b) and (d) assume 8-wagon-long trains with wagon length $L_w = 26.5$ m. Spectrograms are computed over time windows of 20 s with a 90% overlap, and spectra are computed on tapered data (blue traces) in order to avoid the start and the end of the signal where only some of the train wheels are involved (in orange).

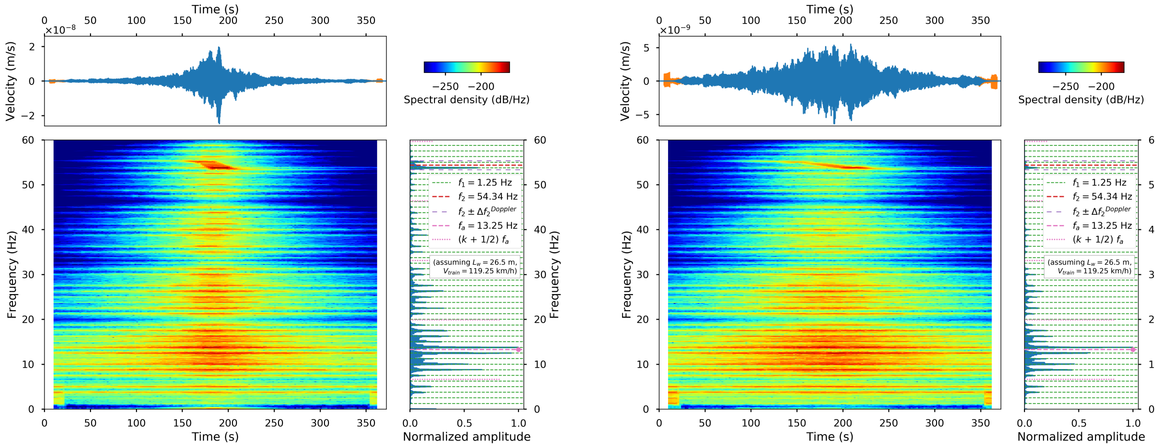

(a) Reference case (Fig. 4c): $V_p = 3400$ m/s, $V_s = 2000$ m/s, $Q_p = 100$, $Q_p = 50$, $d_{min} = 300$ m.

(b) Effect of distance from railway: $V_p = 3400$ m/s, $V_s = 2000$ m/s, $Q_p = 100$, $Q_p = 50$, $d_{min} = 1200$ m.

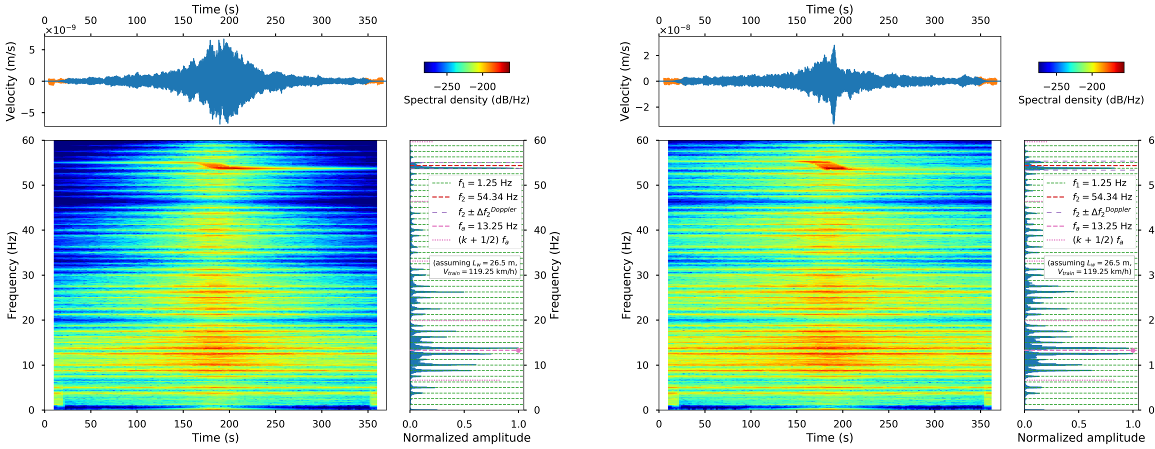

(c) Effect of seismic velocities: $V_p = 5000$ m/s, $V_s = 3000$ m/s, $Q_p = 100$, $Q_p = 50$, $d_{min} = 300$ m.

(d) Effect of attenuation: $V_p = 3400$ m/s, $V_s = 2000$ m/s, $Q_p = 500$, $Q_p = 200$, $d_{min} = 300$ m.

Figure S5: Seismograms (top of each panel), spectrograms (bottom of each panel) and spectra (right of each panel) resulting from train passages over slightly irregular sleepers ($\Delta_{sleeper} = 0.6096 \pm 0.05$ m). All figures assume trains with 8x 26.5-m-long wagons and a train speed $V_{train} = 33.125$ m/s $= 119.25$ km/h. (a) Reference case (same as Fig. 4c): $V_p = 3400$ m/s, $V_s = 2000$ m/s, $Q_p = 100$, $Q_p = 50$, $d_{min} = 300$ m. (b) Effect of distance from railway: $d_{min} = 1200$ m (all other parameters kept the same as reference). (c) Effect of seismic velocities: $V_p = 5000$ m/s, $V_s = 3000$ m/s (all other parameters kept the same as reference). (d) Effect of intrinsic attenuation: $Q_p = 500$, $Q_p = 200$ (all other parameters kept the same as reference). Spectrograms are computed over time windows of 20 s with a 90% overlap, and spectra are computed on tapered data (blue traces) in order to avoid the start and the end of the signal where only some of the train wheels are involved (in orange).

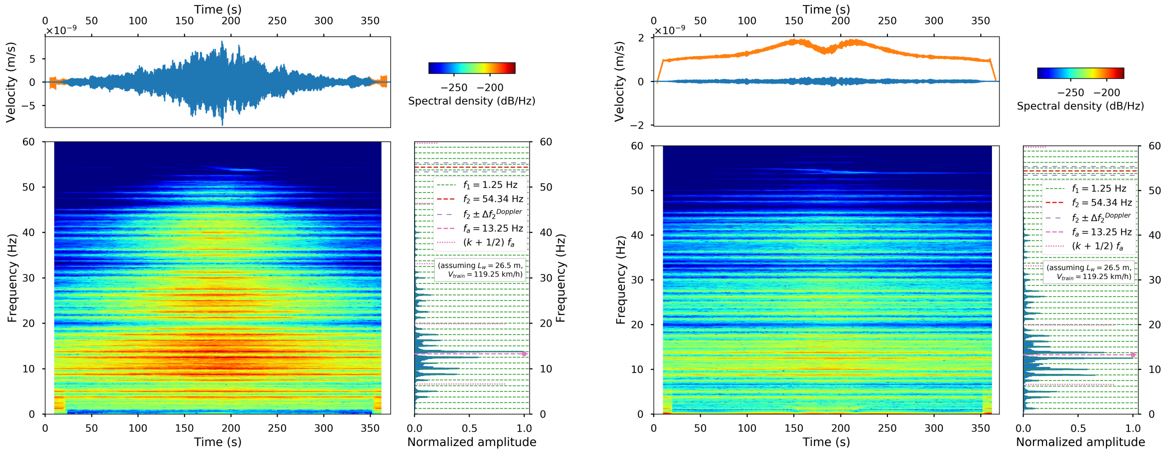

(a) All arrivals (dominated by surface waves).

(b) Refracted P waves only.

Figure S6: Seismograms (top of each panel), spectrograms (bottom of each panel) and spectra (right of each panel) resulting from train passages on slightly irregular sleepers ($\Delta_{sleeper} = 0.6096 \pm 0.05$ m) over a medium where seismic velocities increase with depth ($V_P = 3400$ m/s at the surface to 5000 m/s at 2400 m depth, $V_S = 2000$ m/s at the surface to 3000 m/s at 2400 m depth). Both figures assume trains with 8x 26.5-m-long wagons and a train speed $V_{train} = 33.125$ m/s $= 119.25$ km/h, and a sensor located 1200 m away from the railway. (a) Signal resulting from the convolutions of all arrivals with the train source time functions. (b) Signal resulting from the convolution of the refracted P waves (first arrivals) only. Spectrograms are computed over time windows of 20 s with a 90% overlap, and spectra are computed on tapered data (blue traces) in order to avoid the start and the end of the signal where only some of the train wheels are involved (in orange). In (b), we also apply a highpass filter above 0.5 Hz to remove the quasi-static component (in orange) before computing the spectrum of the blue trace. In order to mitigate computation costs, these results are based on spectral-element simulations valid up to 50 Hz instead of 100 Hz, hence the rapid decay of spectral amplitudes above 50 Hz which makes the f_2-peak barely visible.

References

Alves Costa, P., Calçada, R., Silva Cardoso, A., and Bodare, A. (2010). Influence of soil non-linearity on the dynamic response of high-speed railway tracks. Soil Dynamics and Earthquake Engineering, 30(4):221–235.

Fuchs, F., Bokelmann, G., and the AlpArray Working Group (2018). Equidistant spectral lines in train vibrations. Seismological Research Letters, 89(1):56–66.

Galvín, P., Romero, A., and Domínguez, J. (2010). Fully three-dimensional analysis of high-speed train–track–soil-structure dynamic interaction. Journal of Sound and Vibration, 329(24):5147–5163.

Krylov, V. and Ferguson, C. (1994). Calculation of low-frequency ground vibrations from railway trains. Applied Acoustics, 42(3):199–213.

Li, L., Nimbalkar, S., and Zhong, R. (2018). Finite element model of ballasted railway with infinite boundaries considering effects of moving train loads and Rayleigh waves. Soil Dynamics and Earthquake Engineering, 114:147–153.

Lombaert, G. and Degrande, G. (2009). Ground-borne vibration due to static and dynamic axle loads of InterCity and high-speed trains. Journal of Sound and Vibration, 319(3):1036–1066.

Paderno, C. (2009). Simulation of ballast behaviour under traffic and tamping process. In 9th Swiss Transport Research Conference (STRC 2009).